

Wide range temperature stability of palladium on ceria-praseodymia catalysts for complete methane oxidation

Original

Wide range temperature stability of palladium on ceria-praseodymia catalysts for complete methane oxidation / Ballauri, S.; Sartoretti, E.; Novara, C.; Giorgis, F.; Piumetti, M.; Fino, D.; Russo, N.; Bensaid, S.. - In: CATALYSIS TODAY. - ISSN 0920-5861. - ELETTRONICO. - 390-391:(2022), pp. 185-197. [10.1016/j.cattod.2021.11.035]

Availability:

This version is available at: 11583/2952754 since: 2022-01-24T22:44:13Z

Publisher:

Elsevier B.V.

Published

DOI:10.1016/j.cattod.2021.11.035

Terms of use:

This article is made available under terms and conditions as specified in the corresponding bibliographic description in the repository

Publisher copyright

Elsevier postprint/Author's Accepted Manuscript

© 2022. This manuscript version is made available under the CC-BY-NC-ND 4.0 license
<http://creativecommons.org/licenses/by-nc-nd/4.0/>. The final authenticated version is available online at:
<http://dx.doi.org/10.1016/j.cattod.2021.11.035>

(Article begins on next page)

Wide range temperature stability of palladium on ceria-praseodymia catalysts for complete methane oxidation

Sabrina Ballauri^{a,+}, Enrico Sartoretti^{a,+}, Chiara Novara^a, Fabrizio Giorgis^a, Marco Piumetti^a, Debora Fino^a, Nunzio Russo^a, Samir Bensaid^{a,*}

^a Department of Applied Science and Technology, Politecnico di Torino, Corso Duca degli Abruzzi, 24, 10129 Turin, Italy.

* Corresponding author:

E-mail address: samir.bensaid@polito.it (S. Bensaid).

⁺ These authors contributed equally to this work.

Keywords: methane oxidation, palladium catalysts, ceria-praseodymia, characterization-activity relationships

ABSTRACT

Catalytic oxidation is the most effective technology to control methane emissions from both mobile and stationary sources. Palladium-based materials are widely viewed as the most active catalysts for the methane abatement reaction, even though the high-temperature PdO/Pd transition is linked to a decrease in catalytic activity. Aimed at minimizing this phenomenon, this work compares the catalytic activity and the thermal stability of different Pd-impregnated cerium-praseodymium mixed oxides prepared via Solution Combustion Synthesis. Although the palladium deposition on pure ceria allows obtaining a highly active system, the introduction of praseodymium enhances the thermal stability of the catalyst in an extended temperature range. X-ray photoelectron spectra show that the presence of praseodymium retains Pd in a more oxidized form, thus stabilizing the high-temperature active phase. This effect, as evident from X-ray diffractograms and Raman analyses, was attributed to a strong interaction of palladium particles with praseodymium, thereby hindering their reduction to the metallic form. Moreover, Pr doping played a significant role during methane oxidation in the presence of 5% H₂O, improving both activity and stability compared to Pd on pure ceria. On the whole, Pd/Ce₉₀Pr₁₀ (2 wt% palladium supported on a mixed oxide with a praseodymium content of 10% on a cerium-praseodymium molar basis) was found to be the most promising catalyst amongst the studied materials in both dry and wet conditions, benefitting from the synergistic effect of ceria and praseodymia in improving the Pd activity and stability.

1. Introduction

Natural gas is attracting widespread interest in the automotive and power generation sectors due to the growing awareness of climate change mitigation. It indeed turns out to be the cleanest fossil fuel regarding its poor CO₂, CO, NO_x and SO_x production compared with oil and coal [1]. However, methane is distinguished as a strong greenhouse molecule looking at its Global Warming Potential 28 times higher than carbon dioxide on a 100-year time framework [2,3]. In the context of reducing the environmental impact of methane emissions, catalytic oxidation stands out as the most suitable solution for unburned CH₄ emissions control.

It is generally accepted that supported palladium catalysts are the most effective and active materials for the unburned methane abatement [4,5], even though in the literature some aspects remain unsolved. Additional experimental studies are required to understand the nature of active sites during the typical reaction conditions. Concerning this matter, the negative contribution to the catalytic activity arising from the PdO/Pd transition suggests the importance of palladium oxide at high temperature [6]. On the other side, in the low-temperature range, high methane conversion has been observed on either under-coordinated palladium sites in PdO or metallic palladium [7]. As confirmation, further studies have recognized a mixture of PdO and metallic Pd necessary for methane molecule activation [8,9]. Overall, however, the palladium oxidation, or at least the partial oxidation of its surface, appears to be crucial to obtain a significant activity also in the low-temperature range [10].

In recent years much research has focused on the study of different supports in the interests of obtaining an active and stable catalyst in an extensive temperature range. In this matter, the role of the supports appears to be negligible when compared with the intrinsic activity of palladium species at low temperature [11]. Nevertheless, in accordance with recent works, the extent and the type of interactions between noble metal and support can modify the palladium redox properties, and therefore affect its activity [12]. Conversely, it has been observed that the supports play a more crucial role at high temperature. In this case, palladium-support interactions strongly influence the typical PdO/Pd transformation [13,14]. In this regard, various material such as Al₂O₃, SiO₂, SnO₂ and ZrO₂ have been widely investigated as supports for palladium nanoparticles [11,15,16]. Moreover, other active systems have been obtained by using some transition metal oxides (i.e. Fe₂O₃, NiO and Co₃O₄) as Pd carriers [17]. However, amongst the different materials investigated, the use of ceria as catalytic support has shown great interest over the last decades [13,18,19]. Pd-CeO₂ systems have revealed a mutual improvement in the redox properties of the two species, as well as enhanced reducibility of the systems [20]. Moreover, ceria has proved to increase the thermal stability range of palladium oxide, by promoting fast oxidation of the potentially formed metallic palladium [6,21,22].

Taking into consideration the high activity of Pd/ceria catalysts, in our recent work we have observed that the platinum deposition on equimolar ceria-praseodymia, unlike on pure cerium oxide, is prone to retaining the noble metal in its most oxidized form, even after an extended thermal treatment [23]. Moreover, Fuentes et al. [24] proposed 1 wt% Pd/Ce_{0.9}Ln_{0.1}O_{2-δ} (where Ln = Pr or Gd) as excellent materials for the methane oxidation and the activity was related to high reducibility and strong palladium-support interactions. However, to the best of our knowledge, the interactions between palladium and ceria-praseodymia supports with different composition have not been investigated in the literature yet.

Thus, in this study, we used the SCS method to synthesize cerium-praseodymium mixed oxides with different compositions as catalytic carriers for palladium nanoparticles for methane oxidation. Since in this reaction oxidized palladium species or any part thereof are necessary to obtain high activity and stability, the praseodymium insertion in the ceria lattice appears promising to stabilize the active phase, especially in the high-temperature range. On the whole, the properties resulting from the characterization techniques were correlated with the results of the catalytic activity tests. These latter were carried out in both dry and wet conditions (5 vol% of water in the inner flow) to also examine the role of praseodymium in the well-established severe deactivation of water in the methane oxidation reaction [25–28]. Furthermore, this paper extends the application area of ceria-praseodymia materials, already widely studied for soot and CO oxidation due to their remarkable redox properties [23,29–31].

2. Methods

2.1 Catalyst synthesis

Cerium-praseodymium mixed oxides were prepared through the solution combustion synthesis (SCS) procedure in order to obtain catalytic carriers for the palladium nanoparticles deposition. Throughout this work, the resulting catalysts were denominated as Pd/Ce(100-X)Pr(X), wherein (X) indicates the nominal atomic percentage of Pr in the samples on a Ce-Pr molar basis. The corresponding carriers were referred to as Ce(100-X)Pr(X).

For the preparation of the catalytic supports, prescribed amounts of Ce(NO₃)₃·6H₂O and Pr(NO₃)₃·6H₂O were mixed in 120 mL of deionized water to achieve a total quantity of cation in the final product equal to 17.6 mmol. After adding 3.2 g of urea, the mixture was stirred until the complete dissolution of the various components. Then, the solution was poured into a ceramic crucible and heated to 650 °C for 20 min. Finally, the obtained solid powder was gently ground.

2 wt% palladium-based catalysts were obtained by incipient wetness impregnation starting from the carriers described above. In this respect, 1.5 grams of support were treated using a Pd(NO₃)₂ solution poured dropwise onto the material and subsequently calcined in air at 900 °C for 4 hours.

2.2 Catalyst characterization

The proper Pr/Ce molar ratio of the samples together with the palladium weight percentage were confirmed by using a Thermo Scientific iCAP RQ ICP-MS device. In this regard, powder catalysts were processed in a mixture of nitric acid, hydrochloric acid and hydrogen peroxide at 200 °C for 30 min and afterwards diluted to obtain the suitable metal concentration for the analysis.

The crystallographic structure of powders was determined by X-ray diffraction using a Philips X'Pert PW3040 diffractometer. Diffraction patterns were collected in a 2θ angle range between 20° and 80° using a Cu K α radiation (λ = 1.5419 Å, scan step size = 0.013° and acquisition time of 0.2 seconds per step). The peaks resulting from the diffractograms were assigned in conformity with the Powder Diffraction Files by the International Centre of Diffraction Data (ICDD). The lattice parameter (a) was estimated through the Nelson-Riley extrapolation approach, while the mean size of crystallites was evaluated using Scherrer's formula. With regards to the latter, lanthanum hexaboride (LaB₆) was used as standard material for XRD peak broadening correction.

Porosity and surface area of powders were determined using a Micromeritics Tristar II 3020 apparatus through nitrogen physisorption at -196 °C. Samples were outgassed in nitrogen at 200 °C for 2 h as a thermal treatment prior to the measurement. Specifically, the surface area was evaluated by applying the Brunauer-Emmett-Teller (BET) method and the specific pore volume was determined by the Barrett-Joyner-Halenda (BJH) calculation.

Raman spectroscopy was performed employing a Renishaw InVia micro-Raman spectrometer equipped with a solid-state laser emitting visible light at 514.5 nm. Three room temperature Raman spectra were collected in different points for each sample under a 5x objective, using a 10 mW excitation power and a 225 s acquisition time.

Morphology of both supports and Pd-containing materials was observed through a Zeiss Merlin field emission scanning electron microscope (FESEM) with a Gemini-II lens column.

The surface chemical state of the palladium-based catalysts was investigated through X-ray photoelectron spectroscopy (XPS) using an XPS PHI 5000 Versa Probe instrument (band-pass energy = 187.85 eV, take-off angle = 45° and an X-ray spot size diameter of 100.0 μ m). Spectra deconvolution analysis was then performed to study the relative abundance of the various cations within the superficial catalytic framework.

The catalyst reducibility was evaluated by temperature-programmed reduction with hydrogen using a Thermo Scientific TPDRO 1100 equipped with a TCD detector. As a thermal pre-treatment, catalysts were treated with 20 mL min⁻¹ of oxygen at 550°C for 1 h with the purpose of removing the possible traces of water and/or other physisorbed compounds. In a typical reduction test, 50 mg of sample were exposed to a flow rate of 20 mL min⁻¹ of hydrogen (5 vol%) in Ar by heating the system from 50 to 900 °C.

2.3 Catalytic activity tests

The catalytic activity of both supports and Pd-impregnated catalysts was assessed during the methane oxidation reaction. For this purpose, 50 mg of each material were lightly mixed with 150 mg of silicon carbide to prevent inhomogeneous heating of the catalytic bed. The solid mixture was then placed in a 4 mm inner diameter U-shaped reactor located, in turn, in a PID-controlled furnace. The temperature of the catalytic mixture was monitored by using a thermocouple arranged as close as practicable to the catalytic bed. Samples were pre-treated in air at 100 °C for 30 min ahead of each catalytic test. The latter was commonly performed treating the sample in a 150 mL min⁻¹ flow constituted by 0.3 vol% of CH₄ and 1.2 vol% of O₂ in nitrogen, using a gas hourly space velocity (GHSV) in the range of 60000-80000 h⁻¹. As concerns the palladium-impregnated catalysts, the catalytic tests were also carried out in wet conditions (5 vol% of water added to the inlet flow) through the use of a Bronkhorst Controlled Evaporation and Mixing system (CEM). In all tests, two consecutive heating and cooling cycles were conducted by ramping the system at 5 °C min⁻¹ and by using 100 and 950 °C as starting and final temperature, respectively. Finally, the outgoing flow of the reactor was monitored through two continuous analysers: an ABB AO2020 non-dispersive infrared analyser for CH₄, CO, CO₂ and an Emerson XStream X2GP paramagnetic analyser for O₂ concentration.

3. Results and discussion

3.1 Structural properties of the catalysts

Table 1

Pd, Ce and Pr contents in the palladium-based catalysts analysed via ICP.

Sample	Pd loading (wt%)	Ce content (at%)	Pr content (at%)
Pd/Ce100	1.82	100.0	0.0
Pd/Ce90Pr10	1.58	89.8	10.2
Pd/Ce75Pr25	1.67	75.1	24.9
Pd/Ce50Pr50	1.66	50.4	49.6
Pd/Pr100	1.68	0.0	100.0

The actual Ce and Pr molar content as well as the palladium weight percentage of samples was quantified via ICP analysis. The latter was only carried out on Pd-containing materials taking into account that the noble metal impregnation does not change the Ce-Pr ratio of the starting supports. In this matter, as listed in Table 1, all samples exhibit a measured palladium percentage slightly lower, but quite similar to the nominal loading (2%). In addition, the cerium and praseodymium content results to be practically identical to the theoretical one.

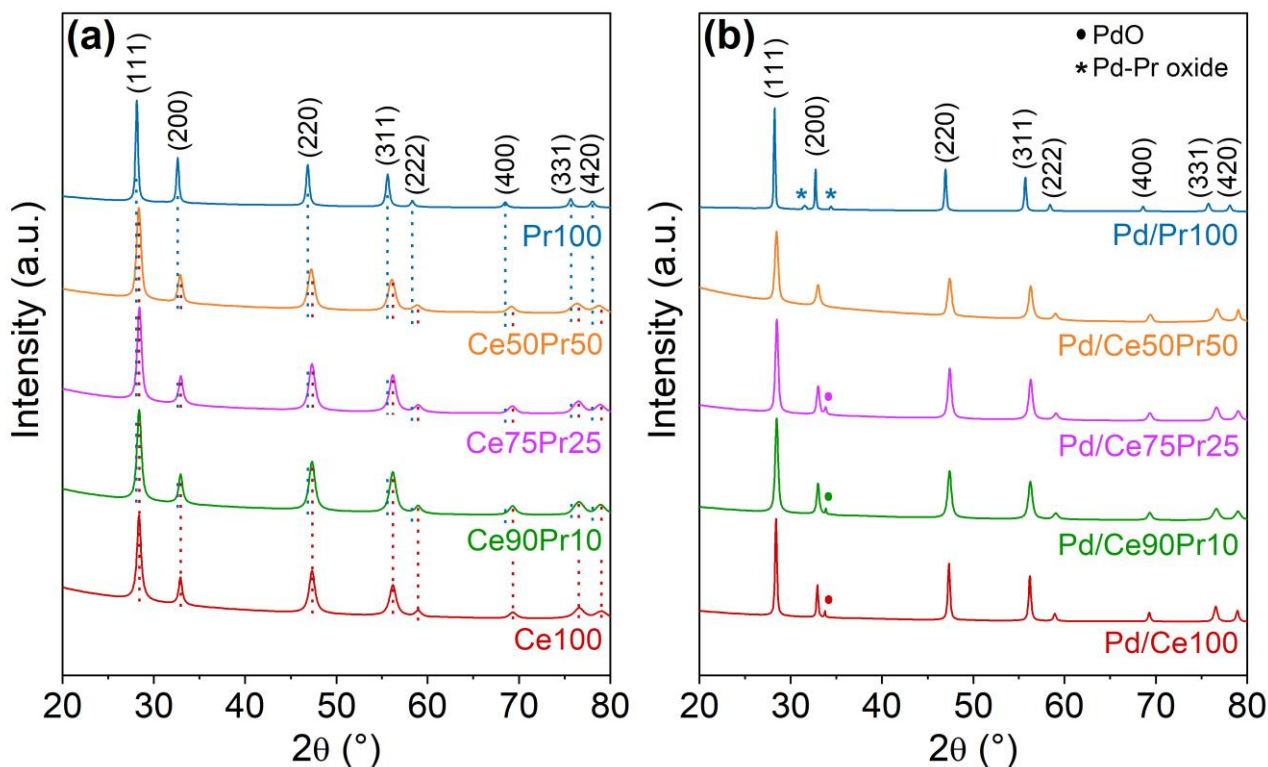


Fig. 1. Powder X-ray diffractograms of supports (a) and Pd-impregnated catalysts (b).

Table 2 summarises the primary structural properties of the powder materials, investigated through XRD, N_2 physisorption and Raman analyses.

Fig. 1 shows the X-ray diffractograms of supports (Fig. 1a) and palladium-containing materials (Fig. 1b). The high similarity between the various patterns is expected due to the close ionic radius value of Ce^{4+} and Pr^{4+} cations [32]. Additionally, the typical cubic fluorite structure of ceria-praseodymia materials is hereby confirmed by the presence of (111), (200), (220), (311), (222), (400), (331) and (420) planes [33,34]. As evident in Fig. 1a, the diffractogram of praseodymia is characterized by peaks centred at smaller angles compared to those of pure cerium oxide and the difference is all the more noticeable when increasing the 2θ value. Concerning cerium-praseodymium mixed oxides, it is noteworthy that samples with low dopant content (Ce90Pr10 e Ce75Pr25) exhibit peak positions nearly identical to those of pure ceria. A shift towards smaller angles was instead observed in the case of equimolar ceria-praseodymia with a value ranging from 0.04 to 0.3° for low and high 2θ values, respectively. Such an effect suggests an elementary cell expansion due to the presence of a greater number of reduced ions in the lattice structure of the materials, as a consequence of the insertion of a high amount of dopant into the ceria framework. On the whole, the limited peak shifts outlined in the diffractograms along with the absence of double peaks arising from phase segregation between the two oxides point out the formation of a solid solution between cerium and praseodymium ions, with dopant ions well embedded in the ceria framework.

As far as the palladium-based materials are concerned, the diffraction patterns of Pd/Ce100, Pd/Ce90Pr10 and Pd/Ce75Pr25 show an additional peak centred at 33.8° (Fig. 1b), which was assigned to the segregation of palladium oxide (JCPDS: 00-041-1107). This feature was instead absent in the Pd/Ce50Pr50 and Pd/Pr100 diffractograms, suggesting that high Pr loading in ceria may be linked either to minor palladium segregation or to the formation of smaller PdO clusters. Interestingly, significant peaks at 31.5° and 34.4° were noted after the palladium deposition on pure praseodymium oxide. According to the literature, they can be attributed to the presence of a palladium-praseodymium mixed phase resulting from an extended high-temperature calcination treatment (at least 900 - 1000°C) [35]. Finally, peaks resulting from the presence of metallic palladium were not detected within all the diffractograms.

Table 2

X-ray diffraction, N_2 physisorption and Raman spectroscopy results for both supports and Pd-impregnated samples.

Sample	X-ray diffraction		N_2 physisorption ^d	Raman
	Crystallite size (nm) ^a	a parameter (nm) ^b	S_{BET} ($\text{m}^2 \text{g}^{-1}$) ^c	$\text{D}/\text{F}_{2\text{g}}$
Ce100	15.8	0.5408	33.1	0.03
Ce90Pr10	14.9	0.5415	17.3	0.74
Ce75Pr25	14.5	0.5419	12.7	1.62
Ce50Pr50	13.4	0.5426	11.4	2.13
Pr100	29.9	0.5469	7.5	-
Pd/Ce100	44.7	0.5414	2.3	0.09
Pd/Ce90Pr10	25.3	0.5414	4.7	1.50
Pd/Ce75Pr25	25.5	0.5412	7.8	2.19
Pd/Ce50Pr50	21.6	0.5407	4.3	3.76
Pd/Pr100	61.0	0.5468	3.5	-

^a Evaluated employing Scherrer's equation.

^b Estimated through the Nelson-Riley extrapolation method [36].

^c Obtained via BET method.

^d Pore volume reported in Table S1.

Regarding the XRD analysis, an important point is the determination of the lattice parameter (a). As regards the catalytic carriers, the lattice parameter value increases with the rising amount of praseodymium in the structure. This effect was expected having regard to the higher ionic radius of Pr^{3+} compared to the tetravalent cations (1.126 for Pr^{3+} in comparison with 0.96 and 0.97 for Pr^{4+} and Ce^{4+} , respectively [37]). In this respect, Vegard's rule can be used as a sound explanation of these findings. Theoretically, the lattice parameter of a solid solution should linearly change with the composition if its value is only linked to the relative size of ions and not to any other phenomena [38]. Fig. 2

represents the variation of the lattice parameter as a function of the praseodymium content in the supports, considering all the samples as a single phase with $\text{Ce}_{1-x}\text{Pr}_x\text{O}_{2-\delta}$ formula. The solid lines are representative of the experimental results, whereas the dashed ones outline the application of Vegard's law to ceria-praseodymia systems according to the work of Rajendran et al. [39]. In detail, the line with a negative slope (Equation 1) shows the lattice parameter variation as a function of the composition when some Ce^{4+} ions are directly replaced with Pr^{4+} ions. Conversely, the line with a positive slope (Equation 2) truthfully describes Ce-Pr systems as a solid solution between CeO_2 and $\text{PrO}_{1.83}$ oxides. The lattice parameters of CeO_2 , PrO_2 and $\text{PrO}_{1.83}$ (0.5411 nm, 0.5392 nm and 0.5470 nm, respectively) were obtained from the crystallographic parameters section of the JCPDS 00-034-0394, JCPDS 00-024-1006 and JCPDS 00-006-0329 files.

$$a_x = -0.00193x + 0.5411 \text{ nm} \quad (1)$$

$$a_x = 0.00582x + 0.5411 \text{ nm} \quad (2)$$

In compliance with Fig. 2, our experimental data result to be between the scissors-like area outlined by the theoretical lines. In detail, these supports give rise to a solid solution quite similar to that formed between CeO_2 and $\text{PrO}_{1.83}$ oxides, suggesting the presence of a non-negligible amount of reduced ions in the material framework, highlighting the high oxygen deficiency of materials.

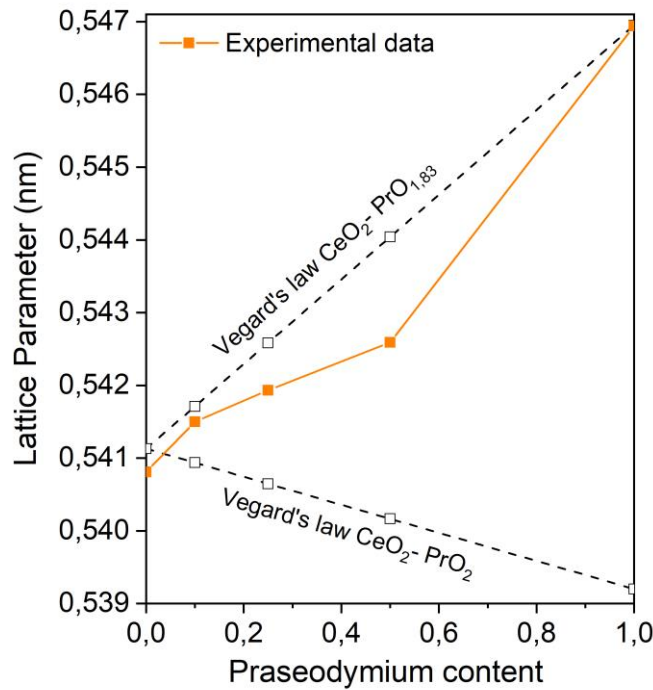


Fig. 2. Theoretical and experimental lattice parameter variation for $\text{Ce}_{1-x}\text{Pr}_x\text{O}_{2-\delta}$ systems as a function of the praseodymium content.

Turning now to the palladium containing catalysts, the Pd/Ce100 sample exhibits a higher a -value compared to the base support. Conversely, the ceria-praseodymia and praseodymia impregnation resulted in a lattice parameter decrease. The variation of the latter is difficult to assess due to the different effects that can simultaneously occur following the Pd introduction and the calcination process. Given that palladium is characterized by a lower ionic radius compared to that of cerium and praseodymium, the a -parameter reduction can be reasonably linked to a direct introduction of palladium, or at least a fraction of it, into the lattice framework of the supports. On the other hand, some authors observed a rise in the a -value when increasing the palladium concentration in systems characterized by the presence of a solid solution with the formula $\text{Pd}_x\text{Ce}_{1-x}\text{O}_2$ [40,41]. This trend is in line with other DFT+U calculations which suggest a structure expansion arising from the substitution of cerium by palladium ions together with the formation of oxygen vacancies [42,43]. Therefore, in case of oxygen vacancy formation, the decrease in the lattice parameter as an effect of the small Pd ionic radius is offset by a network expansion needed for obtaining a stable noble metal position within the catalytic structure.

The outcomes obtained from XRD analyses were also confirmed by Raman spectroscopy, which allowed to further investigate the structural properties of the different samples. The spectra collected on the bare Ce-Pr oxides are reported in Fig. 3a. Pure ceria exhibits an intense F_{2g} peak at 464 cm^{-1} , which was associated with the symmetric stretching mode of the Ce-O bonds in the fluorite structure typical of this oxide [44,45]. Beside this main feature, a less intense Raman band linked to the presence of defects (D band) can also be noticed around 595 cm^{-1} , and it can be ascribed to intrinsic anionic Frenkel sites [44,45]. Analogous spectra were obtained for doped ceria too, albeit with some differences. The presence of the intense F_{2g} mode suggests that Pr ions are well incorporated in ceria lattice even at high dopant loading. However, the progressive shift towards lower wavenumber of the latter component and its asymmetric broadening reveal an increasing structural distortion upon doping [46]. This is consistent with the insertion of numerous Pr^{3+} cations in the ceria framework, as previously evidenced by the progressive shift towards lower 2θ values of XRD patterns when increasing the dopant concentration. Pr^{3+} incorporation causes lattice expansion and the generation of new extrinsic defects, as demonstrated by the much more intense and broader defect band of the mixed oxides. The D band of these samples is centered around $570 - 575\text{ cm}^{-1}$, due to the appearance of new components located at lower wavenumbers which are linked to the formation of extrinsic oxygen vacancies [47,48]. The ratio between the area of the D band and that of the F_{2g} peak was calculated, obtaining an indicative parameter for the defect abundance [45,49]. The D/F_{2g} values, reported in Table 2, show a progressive and remarkable increase upon doping, mainly due to the creation of new defects and vacancies. Nevertheless, other phenomena can also partially account for this rise, although to a lesser extent. Indeed, certain defect sites containing Pr^{4+} ions together with oxygen vacancies are characterized by an enhanced signal at 570 cm^{-1} due to resonance Raman effect [50]. Moreover, the light absorbance of the mixed oxides gradually increases upon Pr addition, thus reducing the light penetration depth, making the Raman spectrum more representative of a superficial region which is commonly richer in vacancies and defects [51].

Fig. 3b displays the Raman spectra acquired on the Pd-containing catalysts. Palladium impregnation and high temperature calcination always result in an increase of the defect abundance of the ceria-based oxides, as evidenced by the higher D/F_{2g} values (Table 2). Furthermore, the addition of Pd is followed by the appearance of new Raman signals. The sharp peak located at 648 cm^{-1} in the spectra of the Pd/Ce100, Pd/Ce90Pr10 and Pd/Ce75Pr25 samples can be ascribed to the B_{1g} vibrational mode of PdO [52]. Hence, the presence of this component points out the formation of a significant quantity of segregated PdO crystals, as also previously evidenced by XRD (Fig. 1b). The higher intensity of the PdO Raman peak of the two Pr-doped samples is probably due to the higher surface-sensitivity of the technique when Ce-Pr mixed oxides are concerned, as previously discussed. On the other hand, the typical feature of PdO is completely absent in the spectra of the Pd/Ce50Pr50 and Pd/Pr100 samples, suggesting that a high Pr content may somehow hinder the formation of those PdO clusters which are large and abundant enough to be detected. However, the latter two samples are characterized by a quite sharp Raman peak appearing at about 498 cm^{-1} after Pd impregnation. Actually, this feature was absent in a spectrum collected on pure praseodymia calcined at the same conditions of the Pd-containing catalysts ($900\text{ }^{\circ}\text{C}$ for 4 h in air). Hence, the appearance of this peak does not seem to be a consequence of the mere calcination procedure, but rather of the addition of palladium. In particular, taking into account the presence of additional peaks at 31.5° and 34.4° in the XRD pattern of Pd/Pr100, this mode could be related to a palladium-praseodymium mixed-phase [35].

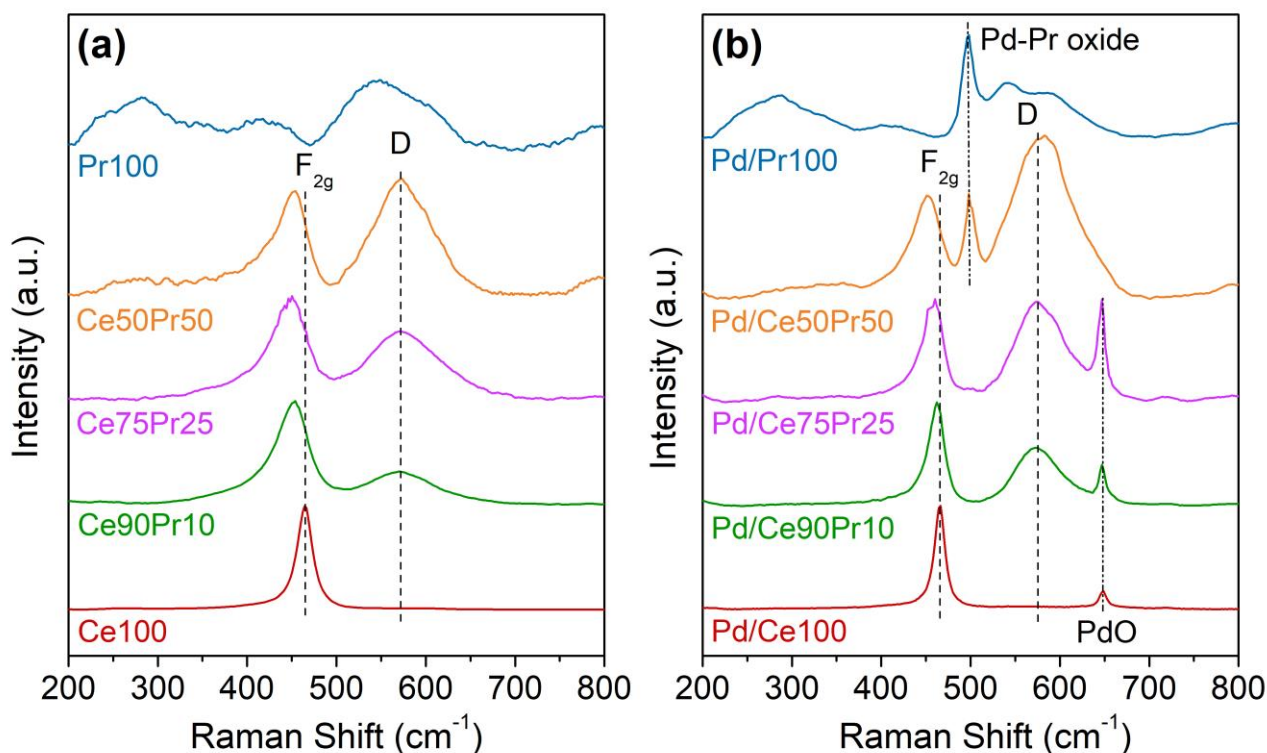


Fig. 3. Raman spectra collected at room temperature on the bare supports (a) and on the Pd-containing catalysts (b), normalized to the F_{2g} intensity. The dashed lines highlight the main Raman modes.

XRD also allowed to estimate the crystallite average dimensions, reported in Table 2. The crystallite size of ceria-praseodymia supports calcined at 650 °C decreases with the rising praseodymium percentage in the sample. This outcome is consistent with other samples having the same composition previously synthesised by our research group [29]. Despite this trend, Ce-Pr supports with a higher praseodymium percentage showed a lower BET surface area. As already observed in the literature [53–55], this signals a crystallite agglomeration phenomenon; accordingly, the particles size estimated through the BET data turns out to be markedly larger than the crystallites size evaluated by Scherrer's equation, especially in the case of carriers with a high praseodymium percentage (data reported in Table S2). Having regard to the rather high surface area of the supports (ranging from 7.5 to 33.1 m² g⁻¹), a substantial reduction in this parameter, matched to a crystallite size increase, was observed in response to the Pd impregnation and the calcination at 900 °C. This effect was expected due to the natural sintering phenomenon arising from the high-temperature treatment. In this respect, Ce100 showed the most pronounced surface area decrease (- 93%), while the Pr-containing catalysts underwent a reduction that varies between -39 and -73%.

Fig. 4 shows the FESEM micrographs of supports and palladium-containing materials. All the samples feature a spongy-like structure resulting from the release of a large quantity of gases during the high-temperature fast reaction between the fuel and the catalytic precursors [56]. The single exception was found in the Pr100 and Pd/Pr100 catalysts, in which a flaky morphology constituted by the overlapping of different plates was observed. The obtainment of rounded particles or flat structures is crucially dependent on the reaction mechanism, which consists of several steps, i.e. solvent evaporation at the beginning of the heating, gel formation and decomposition, self-ignition and lastly, combustion reaction matched with the solid product precipitation and growth. The scarcely-controllable temporal order, as well as the phase in which the different stages occur, lead to the formation of samples with different morphology [57].

The comparison between Figs. 4 a-e and 4 f-j shows that palladium-impregnated catalysts present larger particles than the corresponding supports on account of the high-temperature sintering phenomenon, in agreement with the crystallite size increase previously discussed. Moreover, palladium contributions were not detected in the FESEM images likely to the presence of noble metal clusters with too low dimensions, hardly observable by using this technique.

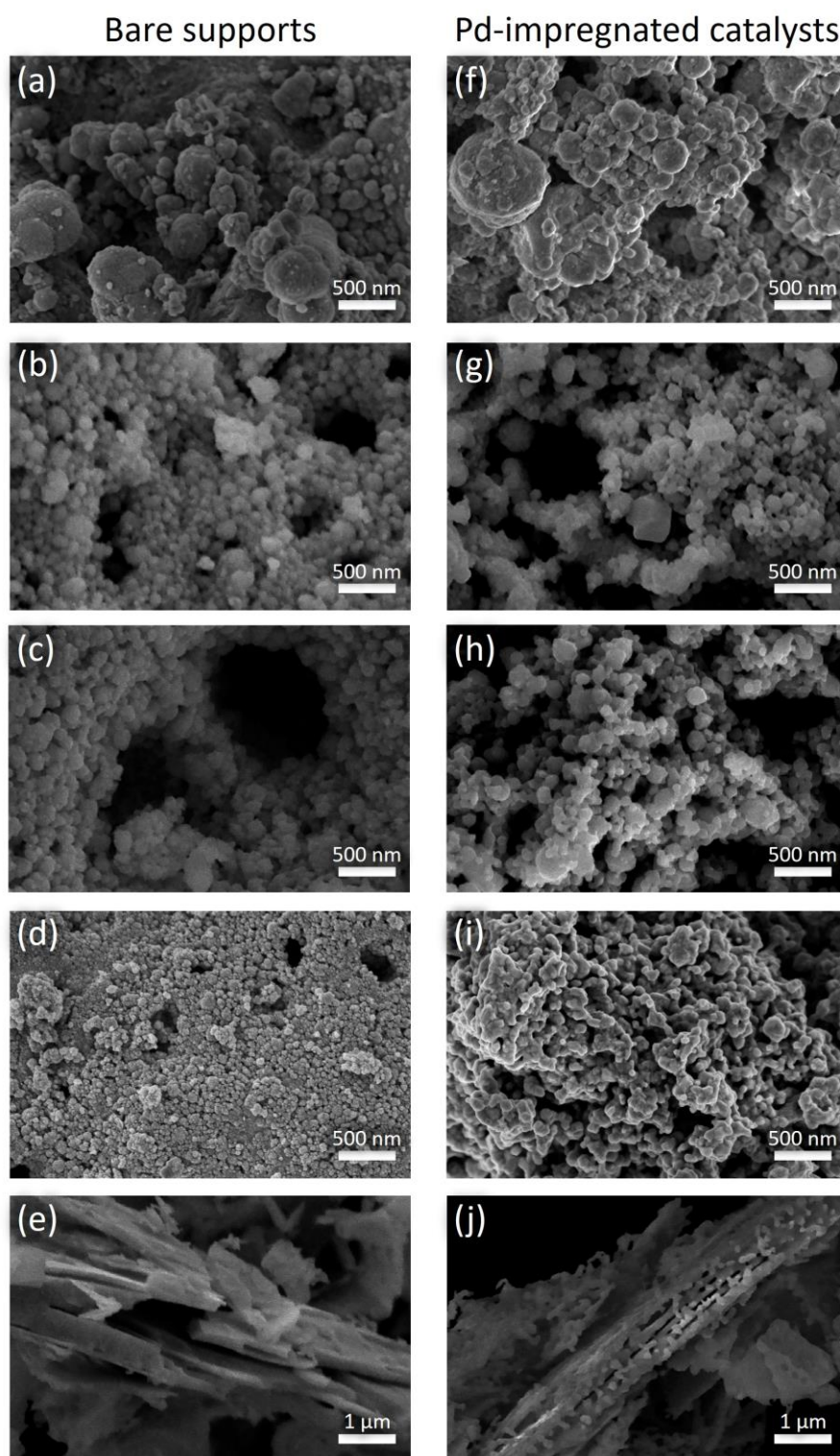


Fig. 4. FESEM images of supports: (a) Ce100, (b) Ce90Pr10, (c) Ce75Pr25, (d) Ce50Pr50, (e) Pr100 and palladium-containing catalysts: (f) Pd/Ce100, (g) Pd/Ce90Pr10, (h) Pd/Ce75Pr25, (i) Pd/Ce50Pr50, (j) Pd/Pr100.

3.2 Surface composition and chemical state

Table 3

Relative abundance (%) of oxygen and palladium species along with Ce and Pr reduced ions.

Sample	O _β	O _α	Ce ³⁺	Pr ³⁺	Pd ⁰	PdO _x (x<1)	Pd ²⁺	Pd ^{(2+γ)+}
Pd/Ce100	64.1	35.9	21.7	-	12.3	42.8	28.1	16.9
Pd/Ce90Pr10	65.9	34.1	20.9	52.8	4.7	23.9	49.9	21.6
Pd/Ce75Pr25	50.0	50.0	19.6	51.7	-	22.3	54.2	23.5
Pd/Ce50Pr50	45.4	54.6	18.1	49.6	-	14.0	58.1	27.9
Pd/Pr100	41.9	58.1	-	48.2	-	10.2	65.2	24.6

XPS analyses were carried out to study the superficial composition and the chemical environment of palladium-based catalysts. More specifically, Fig. 5 illustrates the deconvoluted XPS spectra of powder samples in the O 1s core level region. The lowest binding energy peak, centred at 528.7 eV and herein named as O_β, was ascribed to bulk-like oxygen species [58]. The highest binding energy peak, located at 531.3 eV and herein named as O_α, was instead assigned to other superficial oxygen species such as O⁻, O₂²⁻ and OH⁻ [59,60]. It is worth noting that the O_β position exhibits a shift towards lower binding energy values in praseodymium containing samples. This seems to imply a greater amount of reduced ions in the catalytic framework of Ce-Pr catalysts, given the higher reducibility of the samples (see H₂-TPR results) and the overall trend of decreasing binding energy as the oxidation state decreases [61]. This assumption is also reasonable if considering that elsewhere the peak at 528.5 eV was attributed to Pr₂O₃ [62]. Table 3 summarises the relative abundance of oxygen species resulting from the spectra deconvolution and, as regards the oxygen, the greater the praseodymium percentage is, the more the quantity of O_α species increases. The larger amount of these lower-coordinated oxygen species (with respect to the bulk oxygen) could be linked to superficial defect sites [30,63] that, as detailed in the Raman analysis section (Fig. 3), increase as the dopant percentage in the catalytic framework is raised. A third peak located at ca. 534.3 eV was noted in the oxygen spectra. Although peaks in this binding energy range are usually assigned to weakly adsorbed species [60], they are unlikely to be present considering the high-temperature calcination treatment. Hence, this contribution can be more reasonably ascribed to a palladium 3p peak partially overlapped with the O 1s region [64,65].

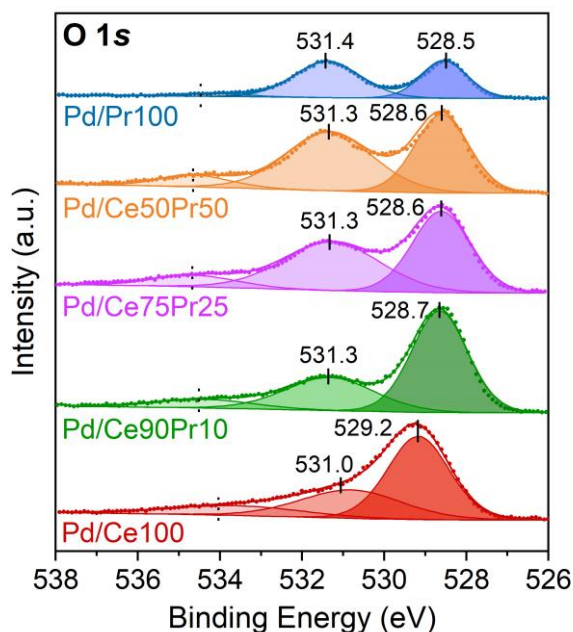


Fig. 5. Deconvoluted X-ray photoelectron spectra of Pd-based catalysts in the O 1s core level region.

Fig. 6 shows the deconvoluted XPS spectra in the Ce 3d and Pr 3d core-level regions. As far as the cerium spectrum is concerned, the deconvolution process was carried out by using 10 peaks labelled with the letters u and v, which refer to the 3d_{3/2} and 3d_{5/2} states, respectively. Two doublets of these peaks (v_o-u_o and v'-u') can be assigned to Ce³⁺, while the remaining ones to the 4+ Ce-oxidation state [66]. According to the work of Poggio-Fraccari et al. [67], a similar

approach was adopted for the analysis of praseodymium spectra: four peaks (a_o - b_o and a' - b') are ascribed to Pr^{3+} and three doublets (b - a , b'' - a'' and b''' - a''') to Pr^{4+} .

The deconvolution outcomes are presented in Table 3. As anticipated from the previous assessment of the lattice parameter (Table 2) and the application of Vegard's law, also the XPS analyses confirm the presence of cerium and praseodymium reduced ions at the surface of the materials. Overall, the cerium and praseodymium 3+ content seems to slightly decrease in praseodymium-rich materials.

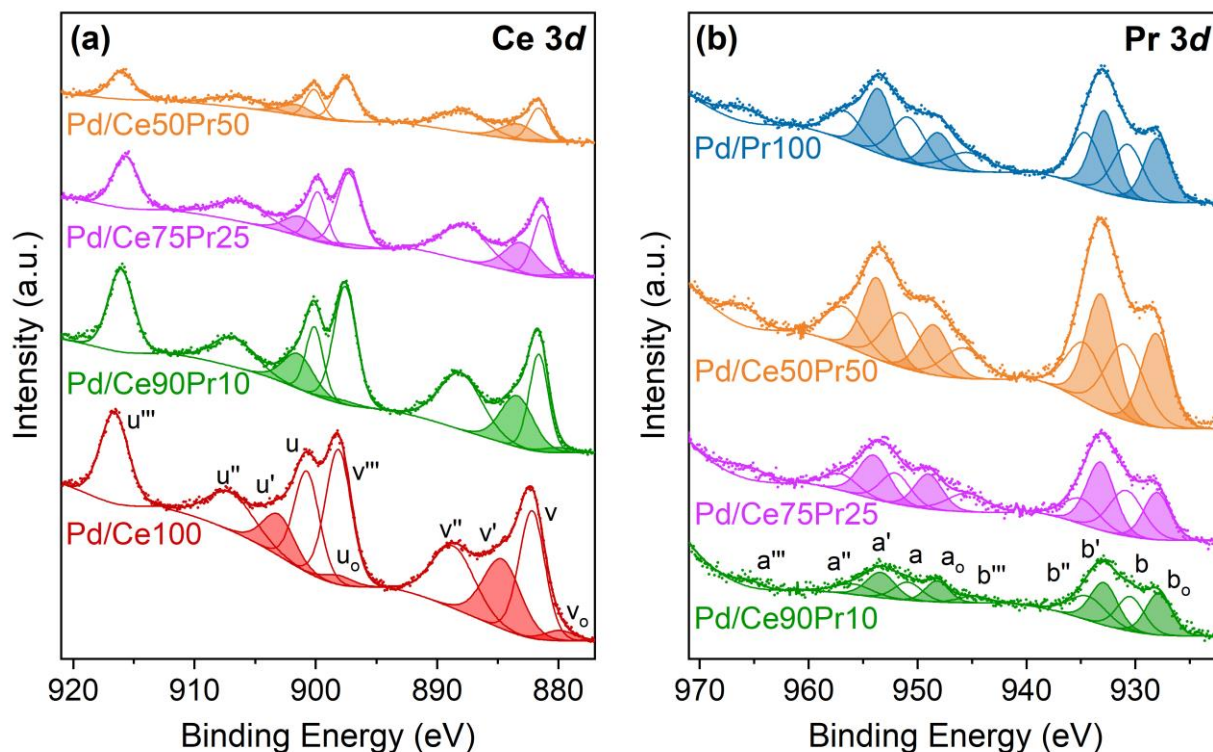


Fig. 6. Deconvoluted X-ray photoelectron spectra of Pd-based catalysts in the Ce 3d (a) and Pr 3d (b) core level regions (coloured peak for reduced oxidation states).

The deconvoluted XP spectra of palladium (Fig. 7) consists of four doublets: (1) metallic Pd at 335.7 eV and 340.4 eV, (2) PdO_x species with $x < 1$ at 336.5 eV and 341.7 eV, (3) Pd^{2+} at 337.5 eV and 342.7 eV and (4) $\text{Pd}^{(2+\delta)+}$ at 338.2 eV and 343.5 eV. The peak assignment was performed in compliance with the literature [68–71]. More specifically, PdO_x refers to a superficial or interfacial palladium oxide characterized by different stoichiometry with respect to the nominal one (PdO), which acts as a redox intermediate in the palladium decomposition/reoxidation process. On the other hand, the $\text{Pd}^{(2+\delta)+}$ component identifies highly oxidized palladium species, suggesting the presence of noble metal ions directly incorporated in the support framework. As shown in Table 3, all the palladium species can be found in the Pd/Ce100 and Pd/Ce90Pr10 spectra (red and green lines in Fig. 7). Strikingly, the metallic palladium fraction goes to zero and the PdO_x concentration becomes meanwhile smaller and smaller as the praseodymium percentage is increased ($\text{Pr} \geq 25\%$). Hence, this confirms our aforementioned theory: praseodymium incorporation into ceria structure is crucial in retaining the impregnated palladium in its more oxidized form.

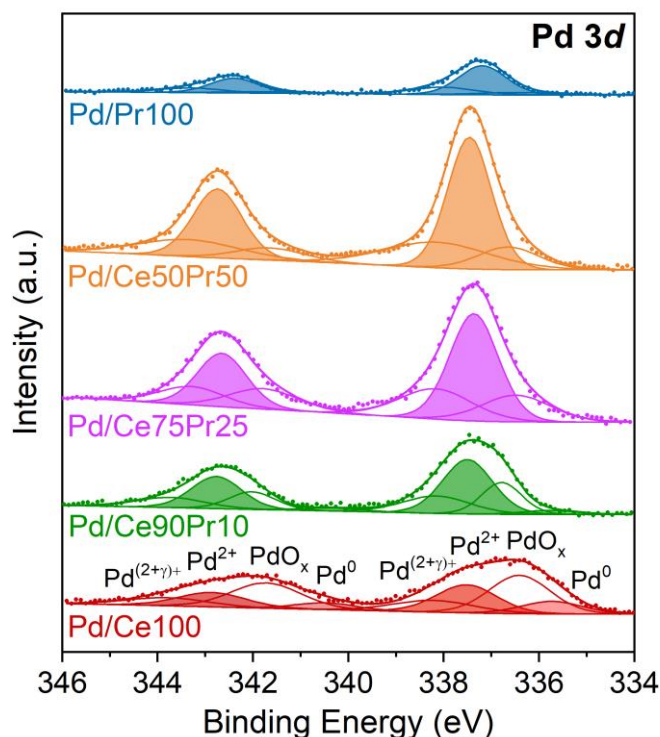


Fig. 7. Deconvoluted X-ray photoelectron spectra of Pd-based catalysts in the Pd 3d core level region (coloured peaks for Pd⁰ and Pd²⁺).

3.3 Reducibility of the catalysts

Table 4

Reducibility of the catalysts in terms of H₂ consumption in the 50-900 °C temperature range.

Sample	H ₂ consumption per g of catalyst (mmol g ⁻¹)
Ce100	0.71
Ce90Pr10	0.69
Ce75Pr25	0.83
Ce50Pr50	1.02
Pr100	1.37
Pd/Ce100	0.20
Pd/Ce90Pr10	1.01
Pd/Ce75Pr25	1.37
Pd/Ce50Pr50	1.44
Pd/Pr100	1.22

Fig. 8 illustrates the hydrogen reduction profiles for the catalytic carriers (Fig. 8a) and the palladium-based materials (Fig. 8b). As concerns the supports, the pure ceria shows a peak centred at 568 °C followed by increasing H₂ consumption in the high-temperature range, generally ascribed to the reduction of the surface and the bulk species, respectively [72]. Ce90Pr10 exhibits a similar behaviour, with two reduction peaks localized at 476 °C and 815 °C. Thus, the introduction of a small amount of praseodymium into the ceria lattice does not significantly alter the reduction profile but reduces the average reduction temperature compared with that of Ce100. Additionally, in line with the literature [73,74], the two bands related to the surface and the bulk reduction were replaced by a marked peak around 400-550 °C in response to the insertion of a higher quantity of praseodymium into the ceria framework (Pr ≥ 25%). As a matter of fact, praseodymium is a more reducible element than cerium and both the typical superficial reduction at

lower temperature and the bulk reduction at high temperature characterizing Ce100 are replaced, in Pr-containing catalysts, with a simultaneous reduction of superficial and bulk species in the low-temperature range (400-550 °C). We also estimated the hydrogen uptake per gram of catalyst throughout the H₂-TPR tests, by integrating the reduction profiles of the samples. As reported in Table 4, the H₂ consumption exhibited by Ce90Pr10 is very similar to that of cerium oxide, but it progressively increases with rising the percentage of praseodymium in the lattice structure of ceria. Therefore, praseodymium promotes the reducibility of the catalysts in terms of lowering the reduction temperature for Ce90Pr10 and lowering the reduction temperature along with increasing the H₂ consumption for the other Pr-doped oxides. Additionally, as discussed in detail in the following section, the greater reducibility of Pr-containing samples with respect to Ce100 is related to their higher catalytic activity. Furthermore, the percentages of tetravalent ions (Ce⁴⁺ + Pr⁴⁺) reduced to trivalent ions during the reduction test were calculated (see Table S3) and found to be similar to those obtained in the literature [72] (for further details see the Supporting Information).

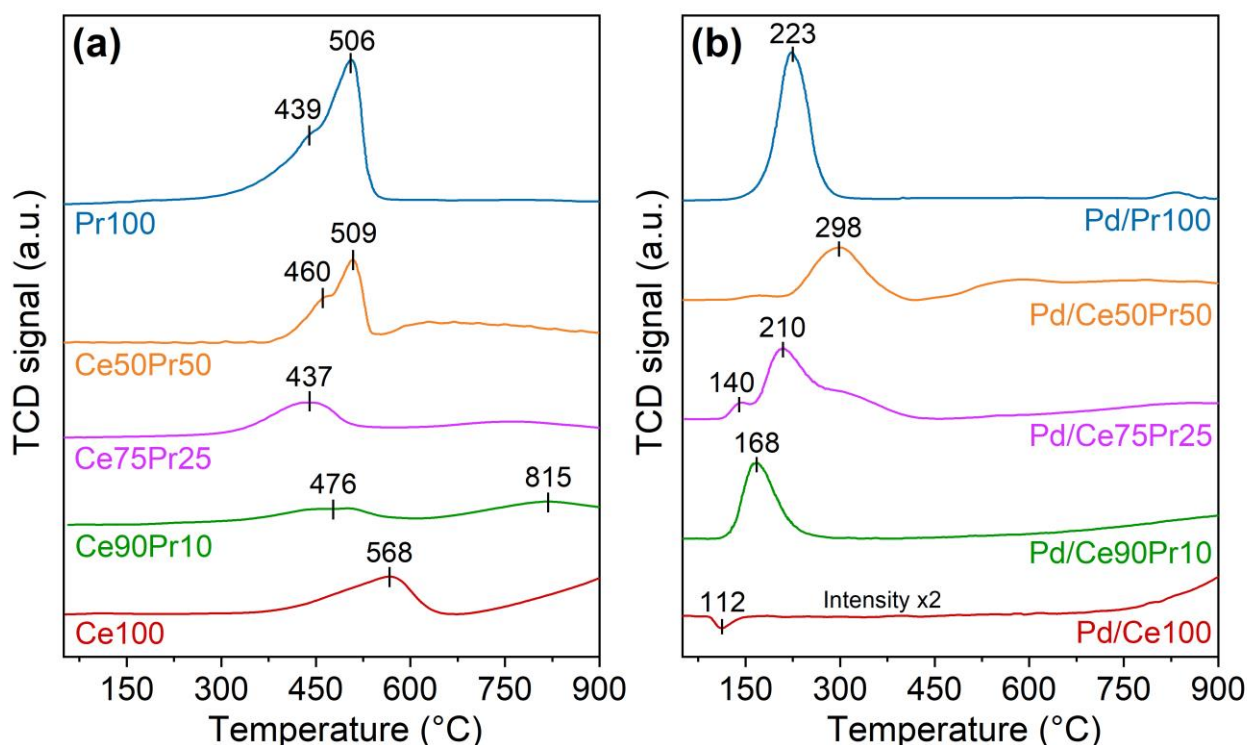


Fig. 8. H₂-TPR profiles of supports (a) and palladium catalysts (b) between 50 and 900 °C.

The reduction profiles of palladium-containing materials are shown in Fig. 8b. Starting from Pd/Ce100, it exhibits a lower H₂ consumption compared with its corresponding support, as evident in Table 4. However, this does not imply lower reducibility of the sample, since further considerations are needed. Firstly, the noble metal increases the ceria reducibility so much to promote its reduction at a temperature lower than 50 °C, which cannot be detected with the used setup [20,75]. Secondly, the Ce100-marked peak centred at 568 °C (red line in Fig. 8a) disappears as a consequence of the Pd-impregnation and calcination process (red line in Fig. 8b). We ascribed this effect to a considerable surface area reduction (-93%, as per Table 2) resulting from the extended high-temperature treatment. Treating a portion of the support with the same thermal process used for the Pd-containing materials (900°C for 4 h), its reduction profile superimposes on that of Pd/Ce100 in the 300 °C to 900 °C temperature range (data not shown). Last but not least, the negative band in the Pd/Ce100 reduction profile was assigned to the formation of a β -hydride palladium phase [76,77].

A different behaviour was noted in response to the palladium deposition on Ce-Pr mixed oxides, which exhibit an intense TPR peak between 160 and 300 °C and a hydrogen consumption higher with respect to that of the corresponding supports. As regard the latter, the hydrogen uptake for the Pd-based materials is greater than the theoretical reduction value of palladium species (0.16 mmol g⁻¹, considering all the noble metal species in the PdO form). It means that palladium improves the support reducibility, both in terms of shifting the reduction band towards a lower temperature and increasing the H₂ consumption. Nevertheless, the reduction temperature of the Pd/Ce-Pr mixed

oxides increases with rising the Pr concentration in the ceria structure. Chun et al. [78] have ascribed this effect to strong interactions between palladium and praseodymium oxides. An exception to this trend seems to occur after the palladium impregnation on pure praseodymium oxide (Pd/Pr100). In fact, the reduction peak of this material is at a lower temperature with respect to that of Pd/Ce50Pr50. An analogous behavior has been observed by Logan et al. [73], probably related to the absence of ceria in the Pd-Pr100 system. Overall, comparing Figs. 8a,b and 10 shows that the palladium impregnation increases the reducibility and the catalytic activity of the supports.

3.4 Catalytic tests

Supports and palladium-based catalysts were tested in order to study their catalytic activity for the methane oxidation reaction. As illustrated by Fig. 9, all the supports performed successfully in the CH₄ oxidation, since their outcomes exceed those observed in the non-catalytic reaction (catalyst replaced with inert silicon carbide). The praseodymium inclusion in the lattice structure of ceria enhances the catalytic activity of the systems since the performances of Ce-Pr mixed oxides and Pr100 are clearly higher than that of Ce100. Indeed, in the case of praseodymium containing catalysts, the temperature at which 50% of methane was converted turned out to be 160-200 °C lower than that of pure ceria. Moreover, although the catalytic activity of the supports follows the trend Ce75Pr25 > Ce50Pr50 > Pr100 > Ce90Pr10 >> Ce100, the difference among the curves of Pr-samples is plenty small compared to that between Pr-samples and pure Ce100. Considering that methane oxidation occurs simultaneously with surface reduction processes, the material reducibility can be directly associated with its catalytic activity [42,79]. Accordingly, higher reducibility induced by the presence of praseodymium (in terms of both lower reduction temperature and higher hydrogen consumption) has a beneficial effect on the catalytic activity of the studied supports, making the performances of Pr-catalysts much higher with regard to that of Ce100. Lastly, all the supports display a high CO₂ selectivity, and this is particularly expected for Pr-samples. As a matter of fact, it was reported elsewhere that only carbon dioxide is detected at the reactor outlet even when methane and oxygen were fed to the reactor at a stoichiometric ratio [80].

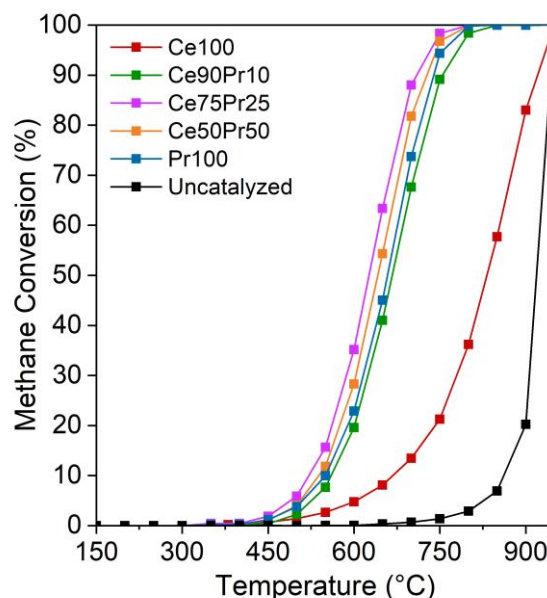


Fig. 9. Methane oxidation light-off curves for ceria, praseodymia and Ce-Pr mixed oxides.

Fig. 10 shows the methane conversion curves of palladium-based catalysts acquired in dry conditions. The second heating (Fig. 10a) and cooling (Fig. 10b) cycle was considered as representative of the catalytic activity of the materials since no substantial changes were observed in the following ones (Fig. S1). As pointed out in Fig. 10, the heating and cooling curves can be divided in two parts: the first one (ranging from 150 to 650 °C) provides information about the activity of the materials, while the second one (ranging from 650 to 900 °C) gives knowledge about their stability.

Looking at the 150-600 °C temperature range, Pd/Ce100 proved to be the most active catalyst. For the sake of comparison, Pd/Ce90Pr10 showed an activity slightly lower, but still very similar to that of Pd/Ce100. Regarding the other compositions, as evident from the reaction rates listed in Table 5, the greater is the dopant content, the more the low-temperature activity decreases. Thus, the addition of a high percentage of praseodymium into the ceria lattice seems to have a detrimental effect in terms of activity. Still about the reaction rates, the values are in agreement with those reported in the literature for Pd/CeO₂ systems obtained through impregnation procedure [81,82]. Conversely, they turn out lower than those of Pd/Co₃O₄, Pd/NiO and Pd/Fe₂O₃ [17] even though Co and Ni oxides are not so appreciated due to their carcinogenicity, while iron oxide could be sensitive to the high temperatures during methane oxidation.

As far as the 650-900 °C temperature range is concerned, the Pd-based catalysts feature a loss of activity, commonly associated to the PdO decomposition to metallic palladium [83]. The high-temperature PdO-Pd transition is a quite complex issue that depends on the oxygen partial pressure and the strength of the palladium-support interactions [13,84]. In this context, we considered the thermal stability as the ability of materials to mitigate the loss of activity at high temperature. As shown in Fig. 10a, the larger loss of activity is observed for Pd/Ce100 and it becomes increasingly less pronounced in materials containing a high praseodymium quantity. The thermal stability of the catalysts is evident also in the cooling cycle (Fig. 10b) in which the extent of the activity loss, and therefore the quantity of Pd species involved into to the PdO-Pd transition, appears as smaller as the Pr content in the catalytic structure increases. Thus, praseodymium sounds promising in preventing the activity loss, maintaining a good PdO thermal stability. On the whole, the best balance between high activity (150-650 °C temperature range) and high thermal stability (650-900 °C temperature range) was observed in Pd/Ce90Pr10, making this sample the most promising catalyst for the methane oxidation reaction.

The greater stability of Pr-catalysts at 650-900 °C is likely due to strong interactions between palladium and praseodymium, that hinder both the noble metal redox cycle and its reduction to the metallic form. Indeed, as reported by Chou et al. [35], the reaction between PdO and PrO_x resulting in the formation of a stable phase shift the PdO-Pd transition to 1220 °C. Throughout this work, strong interactions were especially confirmed in the catalysts with higher dopant content with the formation of a PdO-PrO_x mixed phase (see XRD and Raman spectra, Figs. 1b and 3b). Moreover, the authors of [35] noted that the strong anchorage of PdO by praseodymium, thus its retention in the only Pd²⁺ oxidation state, is adverse in terms of catalytic activity. This is in line with the activity decrease we observed with the increasing dopant percentage into the system and the presence of only oxidized Pd species (Pd²⁺, Pd^{(2+δ)+}) in the XPS spectra of Pr-rich samples (Fig. 7). Hence, the high activity of Pd/Ce100 and Pd/Ce90Pr10 can be related to the presence of palladium in different oxidation states (i.e. Pd⁰, PdO_x, Pd²⁺ and Pd^{(2+δ)+}), identified via XPS analysis (see Fig. 7 and Table 3). In line with the literature, especially in recent years, the simultaneous presence of palladium in the Pd²⁺ form together with more reduced Pd species (Pd⁰, PdO_x) seems to be necessary to obtain high activity at low temperature [6,85].

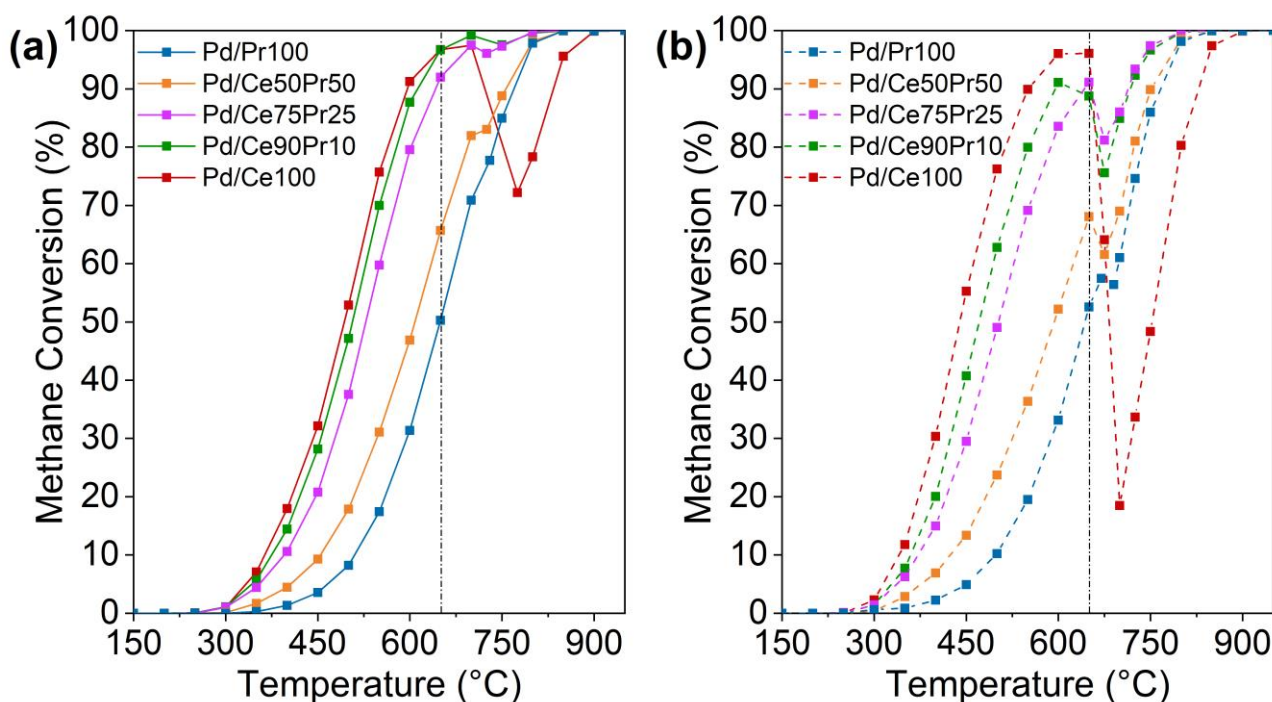


Fig. 10. Methane oxidation light-off curves of palladium-impregnated catalysts in dry conditions in the second heating (a) and cooling (b) cycle.

The outcomes of catalytic methane combustion tests performed in the presence of water can be found in Fig. 11 (Fig. 11a for the heating cycle and Fig. 11 b for the cooling one). It is clear that water plays a detrimental role in CH_4 oxidation throughout the entire temperature range examined. As a matter of fact, during these tests all the catalysts exhibited higher onset temperature and a more pronounced loss of activity at 750-800 °C. As opposed to the dry tests, it is noteworthy that a change in the activity trend can be noted in the presence of water, although the catalytic performance in these conditions is considerably lower (see the reaction rate values in Table 5). In dry conditions, Pd/Ce100 has proved to be the most reactive sample up to 600 °C, while a gradual decrease in activity was observed upon increasing the praseodymium percentage in the ceria structure. Conversely, in the presence of water, Pd/Ce100 exhibits a poorer performance compared to the praseodymium-containing catalysts and, in particular, Pd/Ce90Pr10 is characterized by the best activity. Thus, the water adverse effect seems to be reduced by the dopant addition.

In this context, methane oxidation on palladium-based catalysts proceeds through the consequent breakage of C-H bonds followed by the generation of reduced sites. These latter are then re-oxidized by gaseous or bulk oxygen [86,87]. Considering that, in the case of large quantities of water, the refilling of oxygen from the gas phase is prevented due to the blockage of the active site by OH groups, the oxygen movement across the support-palladium interface plays an important role in the re-oxidation process [87]. Praseodymium-based catalysts, owing to their higher oxygen mobility than ceria [73], eventually promote a quick exchange between bulk oxygen and palladium allowing a fast regeneration of active sites [88]. As a result, Pd/Ce90Pr10 provided the best performances also in the presence of water.

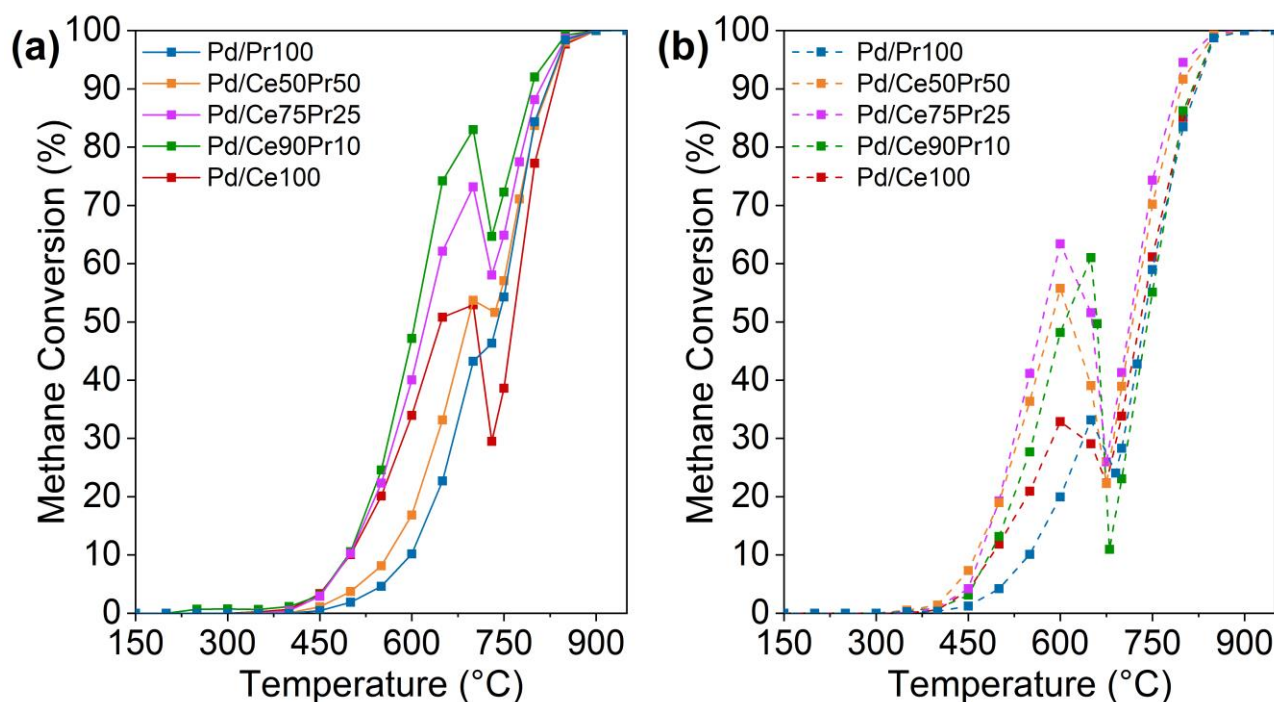


Fig. 11. Light off curves of palladium-impregnated catalysts in wet conditions in the second heating (a) and cooling (b) cycle.

Table 5

Reaction rates for the CH₄ oxidation reaction in dry and wet conditions at 350 and 400 °C, respectively.

Sample	Reaction Rates ($\mu\text{mol CH}_4 \text{ g}_{\text{Pd}}^{-1} \text{ s}^{-1}$)	
	Dry @ 350 °C	Wet @ 400 °C
Pd/Ce100	23.9	2.19
Pd/Ce90Pr10	22.0	4.35
Pd/Ce75Pr25	16.2	1.58
Pd/Ce50Pr50	6.1	0.3
Pd/Pr100	0.9	-

4. Conclusion

In the present work, palladium nanoparticles were deposited on cerium-praseodymium mixed oxides and studied as catalysts for methane oxidation. In particular, the role of praseodymium as dopant in ceria-based supports and its interactions with Pd were investigated.

Characterization techniques revealed the presence of strong interactions between palladium and praseodymium that are particularly emphasized in samples with high dopant content. XRD and Raman analyses outlined indeed the formation of a mixed phase between the PdO and PrO_x oxides, while XPS pointed out the forceful palladium anchorage by praseodymium, which favours Pd retention mainly in the +2-oxidation state.

Comparison of conversion curves obtained in dry conditions revealed that Pd/Ce90Pr10 turns out to be the most promising catalysts among the synthesised materials due to the optimal combination between high activity at low temperature and great thermal stability in the high temperature range. This material sounds promising also in presence of water, being able to reduce the well-known H₂O inhibition effect.

On the whole, this work provides the framework for future studies to better explore the role of praseodymium and the nature of its strong interactions with palladium in the perspective of finding more active and stable catalysts for both dry and wet methane oxidation.

Declaration of interest

The authors declare no competing interests.

Acknowledgments

We would like to thank Camilla Galletti for XRD and ICP-MS analyses, Mauro Raimondo for FESEM images, and Salvatore Guastella for XPS measurement. Elena Valli is gratefully acknowledged for her noteworthy contribution as thesis worker.

Appendix A. Supplementary data

Supplementary material related to this article can be found, in the online version, at doi:

References

- [1] F.-Y. Liang, M. Ryvak, S. Sayeed, N. Zhao, *Chem. Cent. J.* 6 (2012) 1–24.
- [2] D.J. Wuebbles, K. Hayhoe, *Earth-Science Rev.* 57 (2002) 177–210.
- [3] M. Saunois, A.R. Stavert, B. Poulter, P. Bousquet, J.G. Canadell, R.B. Jackson, P.A. Raymond, E.J. Dlugokencky, S. Houweling, *Earth Syst. Sci. Data*. 12 (2020) 1561–1623.
- [4] D. Ciuparu, M.R. Lyubovsky, E. Altman, L.D. Pfefferle, A. Datye, *Catal. Rev. - Sci. Eng.* 44 (2002) 593–649.
- [5] P. G  lin, M. Primet, *Appl. Catal. B Environ.* 39 (2002) 1–37.
- [6] S. Colussi, P. Fornasiero, A. Trovarelli, *Chinese J. Catal.* 41 (2020) 938–950.
- [7] A. Hellman, A. Resta, N.M. Martin, J. Gustafson, A. Trinchero, P.A. Carlsson, O. Balmes, R. Felici, R. Van Rijn, J.W.M. Frenken, J.N. Andersen, E. Lundgren, H. Gr  nbeck, *J. Phys. Chem. Lett.* 3 (2012) 678–682.
- [8] J. Nilsson, P.A. Carlsson, S. Fouladvand, N.M. Martin, J. Gustafson, M.A. Newton, E. Lundgren, H. Gr  nbeck, M. Skoglundh, *ACS Catal.* 5 (2015) 2481–2489.
- [9] Y.X. Xin, B. Yang, H. Wang, S.L. Anderson, C.K. Law, *Proc. Combust. Inst.* 35 (2015) 2233–2240.
- [10] E.D. Goodman, A.A. Ye, A. Aitbekova, O. Mueller, A.R. Riscoe, T. Nguyen Taylor, A.S. Hoffman, A. Boubnov, K.C. Bustillo, M. Nachtegaal, S.R. Bare, M. Cargnello, *J. Chem. Phys.* 151 (2019).
- [11] J.J. Willis, A. Gallo, D. Sokaras, H. Aljama, S.H. Nowak, E.D. Goodman, L. Wu, C.J. Tassone, T.F. Jaramillo, F. Abild-Pedersen, M. Cargnello, *ACS Catal.* 7 (2017) 7810–7821.
- [12] K. Murata, D. Kosuge, J. Ohyama, Y. Mahara, Y. Yamamoto, S. Arai, A. Satsuma, *ACS Catal.* 10 (2020) 1381–1387.
- [13] R.J. Farrauto, J.K. Lampert, M.C. Hobson, E.M. Waterman, *Appl. Catal. B, Environ.* 6 (1995) 263–270.
- [14] M. Cargnello, J.J. Delgado Ja  n, J.C. Hern  ndez Garrido, K. Bakhmutsky, T. Montini, J.J. Calvino G  mez, R.J. Gorte, P. Fornasiero, *Science*. 337 (2012) 713–717.
- [15] J.H. Park, J.H. Cho, Y.J. Kim, E.S. Kim, H.S. Han, C.H. Shin, *Appl. Catal. B Environ.* 160–161 (2014) 135–143.
- [16] K. Eguchi, H. Arai, *Appl. Catal. A Gen.* 222 (2001) 359–367.
- [17] D. Seeburg, D. Liu, J. Radnik, H. Atia, M.M. Pohl, M. Schneider, A. Martin, S. Wohlrab, *Catalysts*. 8 (2018).
- [18] S. Colussi, A. Trovarelli, C. Cristiani, L. Lietti, G. Groppi, *Catal. Today*. 180 (2012) 124–130.
- [19] T.P. Senftle, A.C.T. Van Duin, M.J. Janik, *ACS Catal.* 7 (2017) 327–332.
- [20] D. Kaya, D. Singh, S. Kincal, D. Uner, *Catal. Today*. 323 (2019) 141–147.
- [21] G. Groppi, C. Cristiani, L. Lietti, C. Ramella, M. Valentini, P. Forzatti, *Catal. Today*. 50 (1999) 399–412.
- [22] P.O. Thevenin, A. Alcalde, L.J. Pettersson, S.G. J  r  s, J.L.G. Fierro, *J. Catal.* 215 (2003) 78–86.
- [23] T. Andana, M. Piumetti, S. Bensaid, L. Veyre, C. Thieuleux, N. Russo, D. Fino, E.A. Quadrelli, R. Pirone, *Appl. Catal. B Environ.* 226 (2018) 147–161.
- [24] R.O. Fuentes, L.M. Ac   a, A.G. Leyva, R.T. Baker, H. Pan, X. Chen, J.J. Delgado-Ja  n, *J. Mater. Chem. A*. 6 (2018) 7488–7499.
- [25] J.C. Van Giezen, F.R. Van Den Berg, J.L. Kleinen, A.J. Van Dillen, J.W. Geus, *Catal. Today*. 47 (1999) 287–293.
- [26] K. Persson, L.D. Pfefferle, W. Schwartz, A. Ersson, S.G. J  r  s, *Appl. Catal. B Environ.* 74 (2007) 242–250.
- [27] M. Monai, T. Montini, C. Chen, E. Fonda, R.J. Gorte, P. Fornasiero, *ChemCatChem*. 7 (2015) 2038–2046.
- [28] W. Huang, E.D. Goodman, P. Losch, M. Cargnello, *Ind. Eng. Chem. Res.* 57 (2018) 10261–10268.
- [29] T. Andana, M. Piumetti, S. Bensaid, N. Russo, D. Fino, R. Pirone, *Appl. Catal. B Environ.* 197 (2016) 125–137.

- [30] T. Andana, M. Piumetti, S. Bensaid, N. Russo, D. Fino, *Appl. Catal. A Gen.* 583 (2019) 117136.
- [31] E. Sartoretti, D. Fino, F. Martini, M. Piumetti, S. Bensaid, N. Russo, *Catalysts*. 10 (2020).
- [32] B.M. Reddy, G. Thirumurthulu, L. Katta, Y. Yamada, S.E. Park, *J. Phys. Chem. C*. 113 (2009) 15882–15890.
- [33] S.C. Laha, R. Ryoo, *Chem. Commun.* 3 (2003) 2138–2139.
- [34] F. Bondioli, A.M. Ferrari, L. Lusvarghi, T. Manfredini, S. Nannarone, L. Pasquali, G. Selvaggi, *J. Mater. Chem.* 15 (2005) 1061–1066.
- [35] T.C. Chou, T. Kennelly, R.J. Farrauto, US Patent 5 169 300: Praseodymium-palladium binary oxide, catalyst, methods of combustion and regeneration, 1992.
- [36] J.B. Nelson, D.P. Riley, *Proc. Phys. Soc.* 57 (1945) 160–177.
- [37] R.D. Shannon, *Acta Cryst.* 32 (1976) 751–767.
- [38] A.R. West, *Crystal Defects, Non-Stoichiometry and Solid Solutions*, in: *Solid State Chem.*, 2014: pp. 83–124.
- [39] M. Rajendran, K.K. Mallick, A.K. Bhattacharya, *J. Mater. Sci.* 33 (1998) 5001–5006.
- [40] L.M. Misch, J.A. Kurzman, A.R. Derk, Y. Il Kim, R. Seshadri, H. Metiu, E.W. McFarland, G.D. Stucky, *Chem. Mater.* 23 (2011) 5432–5439.
- [41] P. Singh, M.S. Hegde, *Cryst. Growth Des.* 10 (2010) 2995–3004.
- [42] A.D. Mayernick, M.J. Janik, *J. Phys. Chem. C*. 112 (2008) 14955–14964.
- [43] C.I. Hiley, J.M. Fisher, D. Thompson, R.J. Kashtiban, J. Sloan, R.I. Walton, *J. Mater. Chem. A*. 3 (2015) 13072–13079.
- [44] S. Agarwal, X. Zhu, E.J.M. Hensen, L. Lefferts, B.L. Mojet, *J. Phys. Chem. C*. 118 (2014) 4131–4142.
- [45] E. Sartoretti, C. Novara, F. Giorgis, M. Piumetti, S. Bensaid, N. Russo, D. Fino, *Sci. Rep.* 9 (2019) 3875.
- [46] N. Guillén-Hurtado, J. Giménez-Mañogil, J.C. Martínez-Munuera, A. Bueno-López, A. García-García, *Appl. Catal. A Gen.* 590 (2020) 117339.
- [47] J.C. Martínez-Munuera, M. Zoccoli, J. Giménez-Mañogil, A. García-García, *Appl. Catal. B Environ.* 245 (2019) 706–720.
- [48] E. Sartoretti, C. Novara, M. Fontana, F. Giorgis, M. Piumetti, S. Bensaid, N. Russo, D. Fino, *Appl. Catal. A Gen.* 596 (2020) 117517.
- [49] M. Lykaki, E. Pachatouridou, S.A.C. Carabineiro, E. Iliopoulou, C. Andriopoulou, N. Kallithrakas-Kontos, S. Boghosian, M. Konsolakis, *Appl. Catal. B Environ.* 230 (2018) 18–28.
- [50] A. Westermann, C. Geantet, P. Vernoux, S. Lorient, J. Raman Spectrosc. 47 (2016) 1276–1279.
- [51] S. Bensaid, M. Piumetti, C. Novara, F. Giorgis, A. Chiodoni, N. Russo, D. Fino, *Nanoscale Res. Lett.* 11 (2016) 1–14.
- [52] A. Baylet, P. Marécot, D. Duprez, P. Castellazzi, G. Groppi, P. Forzatti, *Phys. Chem. Chem. Phys.* 13 (2011) 4607–4613.
- [53] A.I.Y. Tok, S.W. Du, F.Y.C. Boey, W.K. Chong, *Mater. Sci. Eng. A*. 466 (2007) 223–229.
- [54] E. Poggio-Fraccari, F. Mariño, M. Laborde, G. Baronetti, *Appl. Catal. A Gen.* 460–461 (2013) 15–20.
- [55] E. Poggio-Fraccari, B. Irigoyen, G. Baronetti, F. Mariño, *Appl. Catal. A Gen.* 485 (2014) 123–132.
- [56] S. Patil, H.P. Dasari, *Mater. Sci. Energy Technol.* 2 (2019) 485–489.
- [57] A. Varma, A.S. Mukasyan, A.S. Rogachev, K. V. Manukyan, *Chem. Rev.* 116 (2016) 14493–14586.
- [58] G. Grzybek, P. Stelmachowski, S. Gudyka, P. Indyka, Z. Sojka, N. Guillén-Hurtado, V. Rico-Pérez, A. Bueno-López, A. Kotarba, *Appl. Catal. B Environ.* 180 (2016) 622–629.
- [59] F.H. Scholes, A.E. Hughes, S.G. Hardin, P. Lynch, P.R. Miller, *Chem. Mater.* 19 (2007) 2321–2328.
- [60] J.C. Dupin, D. Gonbeau, P. Vinatier, A. Levasseur, *Phys. Chem. Chem. Phys.* 2 (2000) 1319–1324.
- [61] F.A. Stevie, C.L. Donley, *J. Vac. Sci. Technol. A*. 38 (2020) 063204.
- [62] H. Al Kutubi, L. Rassaei, W. Olthuis, G.W. Nelson, J.S. Foord, P. Holdway, M. Carta, R. Malpass-Evans, N.B. McKeown, S.C. Tsang, R. Castaing, T.R. Forder, M.D. Jones, D. He, F. Marken, *RSC Adv.* 5 (2015) 73323–73326.
- [63] L. Soler, A. Casanovas, C. Escudero, V. Pérez-Dieste, E. Aneggi, A. Trovarelli, J. Llorca, *ChemCatChem*. 8 (2016) 2748–2751.
- [64] D. Mandal, K.J. Kim, J.S. Lee, *Langmuir*. 28 (2012) 10310–10317.
- [65] L.S. Kibis, A.I. Titkov, A.I. Stadnichenko, S. V. Koscheev, A.I. Boronin, *Appl. Surf. Sci.* 255 (2009) 9248–9254.
- [66] B.M. Reddy, A. Khan, Y. Yamada, T. Kobayashi, S. Lorient, J.-C. Volta, *J. Phys. Chem. B*. 107 (2003) 5162–5167.
- [67] E. Poggio-Fraccari, G. Baronetti, F. Mariño, *J. Electron Spectrosc. Relat. Phenomena*. 222 (2018) 1–4.
- [68] T. Pillo, R. Zimmermann, P. Steiner, S. Hüfner, *J. Phys. Condens. Matter*. 9 (1997) 3987–3999.
- [69] S. Colussi, A. Trovarelli, E. Vesselli, A. Baraldi, G. Comelli, G. Groppi, J. Llorca, *Appl. Catal. A Gen.* 390 (2010) 1–10.
- [70] L.S. Kibis, A.I. Stadnichenko, S. V Koscheev, V.I. Zaikovskii, A.I. Boronin, *J. Phys. Chem. C*. 116 (2012) 19342–19348.
- [71] K.R. Priolkar, P. Bera, P.R. Sarode, M.S. Hegde, S. Emura, R. Kumashiro, N.P. Lalla, *Chem. Mater.* 14 (2002) 2120–2128.

- [72] B. De Rivas, N. Guillén-Hurtado, R. López-Fonseca, F. Coloma-Pascual, A. García-García, J.I. Gutiérrez-Ortiz, A. Bueno-López, *Appl. Catal. B Environ.* 121–122 (2012) 162–170.
- [73] A.D. Logan, M. Shelef, *J. Mater. Res.* 9 (1994) 468–475.
- [74] J. Giménez-Mañogil, N. Guillén-Hurtado, S. Fernández-García, X. Chen, J.J. Calvino-Gámez, A. García-García, *Top. Catal.* 59 (2016) 1065–1070.
- [75] R. de S. Monteiro, F.B. Noronha, L.C. Dieguez, M. Schmal, *Appl. Catal. A, Gen.* 131 (1995) 89–106.
- [76] H. Lieske, J. Völter, *J. Phys. Chem.* 89 (1985) 1841–1842.
- [77] V. Ferrer, A. Moronta, J. Sanchez, R. Solano, S. Bernal, D. Finol, *Catal. Today* 108 (2005) 487–492.
- [78] W. Chun, G.W. Graham, J.A. Lupescu, R.W. McCabe, M.M. Koranne, R. Brezny, *Catal. Letters.* 106 (2006) 95–100.
- [79] M.F. Luo, Z.L. Yan, L.Y. Jin, *J. Mol. Catal. A Chem.* 260 (2006) 157–162.
- [80] P. Sonström, J. Birkenstock, Y. Borchert, L. Schilinsky, P. Behrend, K. Gries, K. Müller, A. Rosenauer, M. Bäumer, *ChemCatChem.* 2 (2010) 694–704.
- [81] A. Toso, S. Colussi, S. Padigapaty, C. de Leitenburg, A. Trovarelli, *Appl. Catal. B Environ.* 230 (2018) 237–245.
- [82] M. Danielis, S. Colussi, C. de Leitenburg, L. Soler, J. Llorca, A. Trovarelli, *Angew. Chemie - Int. Ed.* 57 (2018) 10212–10216.
- [83] R.J. Farrauto, M.C. Hobson, T. Kennelly, E.M. Waterman, *Appl. Catal. A, Gen.* 81 (1992) 227–237.
- [84] S.K. Matam, M.H. Aguirre, A. Weidenkaff, D. Ferri, *J. Phys. Chem. C.* 114 (2010) 9439–9443.
- [85] M. Danielis, S. Colussi, C. de Leitenburg, A. Trovarelli, *Catal. Commun.* 135 (2020) 105899.
- [86] A.D. Mayernick, M.J. Janik, *J. Catal.* 278 (2011) 16–25.
- [87] D. Ciuparu, L. Pfefferle, *Catal. Today.* 77 (2002) 167–179.
- [88] D. Ciuparu, E. Perkins, L. Pfefferle, *Appl. Catal. A Gen.* 263 (2004) 145–153.